Sensors & Diagnostics

PAPER

View Article Online
View Journal | View Issue

Cite this: *Sens. Diagn.*, 2024, **3**, 256

Enhanced mechanical and electrical properties of starch-based hydrogels incorporating polyacrylic acid and MXene for advanced wearable sensors in sign language recognition†

Jionghong Liang,[ab] Ke Ma,[a] Wenshuo Gao,[a] Yue Xin, *[a] Shousen Chen,[a] Weicheng Qiu,[a] Gengzhe Shen[c] and Xin He *[a]

Received 21st September 2023,
Accepted 24th November 2023

DOI: 10.1039/d3sd00250k

rsc.li/sensors

Traditional starch-based hydrogels often lack the mechanical robustness and electrical conductivity required for strain sensing applications. In this study, a conductive organohydrogel was developed by blending starch and MXene with polyacrylic acid (PAA). The resulting PAA/starch/MXene organohydrogel exhibits exceptional mechanical strength, high electrical conductivity, robust adhesion, and resilience to low temperatures. Strain sensors based on this innovative material demonstrate remarkable characteristics, including high sensitivity (maximum GF = 14.19), rapid response time (approximately 160 ms), a wide sensing range (exceeding 800%), and excellent cycling stability. Notably, these sensors remain efficient even at frigid temperatures as low as −30 °C. Furthermore, these sensors find practical application in sign language translation, achieving an impressive recognition rate of up to 100% for complex sentences. When integrated into a sensor array, they enable precise assessment of load magnitude and distribution. Consequently, this research introduces an innovative strategy for fabricating highly efficient conductive hydrogels, holding significant promise for diverse applications in the realm of flexible electronic devices, and promoting sustainable advancements in the field of wearable electronics.

1 Introduction

In recent times, there has been a growing interest in flexible and wearable strain sensors due to their ability to real-time monitor human motion and physiological signals.[1–9] Conductive hydrogels, known for their stretchability, biocompatibility, tunable chemical composition and structure, as well as sensitivity to strain, hold significant promise for a wide range of applications in wearable electronics.[10–14] However, these conductive hydrogel-based sensors face certain limitations that hinder their utility as high-performance wearable devices. For instance, they often require external tapes or adhesives to attach to the skin for monitoring, resulting in discomfort and inaccuracies in motion and physiological signal acquisition.[15–20] Additionally, these sensors exhibit limited fatigue tolerance, leading to reduced cycle stability and a short lifespan, especially in sub-zero working conditions.[21–25] Pure water-based conductive hydrogels are susceptible to freezing, causing rigidity, loss of conductivity, and reduced flexibility.[26–28] Hence, there is a critical need to develop conductive hydrogel materials with repetitive adhesion, high stretchability, sensitivity, antifreeze properties, and fatigue resistance.

To promote sustainable development, researchers are turning to natural polymers and biodegradable, biocompatible synthetic polymers for hydrogel fabrication. Starch, due to its biodegradability, cost-effectiveness, abundance, renewability, and high viscosity, stands out as an attractive option.[29–31] Gelatinization of starch disrupts its crystalline structure,[32,33] resulting in an increased number of free hydroxyl groups and higher viscosity, which can enhance hydrogel adhesion to various materials.[34,35] Nevertheless, the rigid macromolecular chains in starch-derived hydrogels often lead to poor mechanical properties.[36–41] Furthermore, native starch has low conductivity, rendering it unsuitable for strain sensors. Fortunately, combining starch with other hydrophilic polymers and conductive inorganic materials can improve these properties through physical or chemical interactions.[42–44] For example, Lin *et al.* developed a

[a] *School of Applied Physics and Materials, Wuyi University, Jiangmen 529020, P.R. China. E-mail: xin3231946@163.com, hexin@wyu.edu.cn*
[b] *School of Electromechanical Engineering, Guangdong University of Technology, Guangzhou 510006, P.R. China*
[c] *Zhuhai Institute of Advanced Technology Chinese Academy of Sciences, Zhuhai 519003, P.R. China*

† Electronic supplementary information (ESI) available. See DOI: https://doi.org/10.1039/d3sd00250k

stretchable and self-healing double-network (DN) hydrogel composed of hydroxypropyl starch (HPS) and sodium alginate (SA), which exhibited an 80-fold increase in storage modulus compared to HPS hydrogels.[45] Similarly, Depa *et al.* reported a double-filled nanocomposite hydrogel made from poly(*N*-isopropylacrylamide) (PNIPAm), SiO_2, and starch, demonstrating improved mechanical properties due to the interaction of starch's hydroxyl groups with the PNIPAm matrix and SiO_2 nanofiller.[46] Additionally, starch-based hydrogels can function as strain sensors when conductive nanoparticles, such as metal particles or carbon materials, are incorporated into the hydrogel structure to form a conductive network.[47,48] However, challenges remain, such as achieving uniform dispersion of inorganic electrical materials in starch-based hydrogels, which can often lead to reduced conductivity of the starch network.

MXene, a two-dimensional material, possesses impressive mechanical, hydrophilic, and conductive properties. Its high specific surface area and abundance of surface functional groups (*e.g.*, –O, –F, and –OH) enable MXene nanosheets to interact with hydrophilic polymer chains *via* hydrogen bonding or electrostatic forces, forming a three-dimensional conductive pathway within hydrogel networks.[49,50] This makes MXene-based hydrogels suitable for use in flexible wearable electronics, as they can provide both satisfactory mechanical and sensing performance. For example, Zhang *et al.* developed a hydrogel strain sensor with a remarkable stretchability exceeding 3400% and a high gauge factor of 25 by incorporating MXene into poly(vinyl alcohol) (PVA) hydrogel, enabling the detection of motion direction and speed.[51] Luan *et al.* also created a composite double network hydrogel composed of polyacrylamide (PAM) and sodium alginate (SA), capable of monitoring human motion, recognizing handwriting, and facilitating real-time human–computer interaction.[52]

This study presents the development of a conductive organohydrogel by combining starch and MXene with polyacrylic acid (PAA), resulting in outstanding mechanical properties, anti-freezing capabilities, self-adhesion, and strain sensing capabilities. The presence of numerous hydrogen bonding and electrostatic interactions among the components creates a densely and uniformly conductive three-dimensional network, leading to enhanced mechanical strength and conductivity. The PAA/starch/MXene organohydrogel exhibits excellent mechanical strength, electrical conductivity, strong adhesion, and low-temperature performance. Furthermore, the PAA/starch/MXene organohydrogel-based sensor demonstrates high sensitivity (14.19 at 400% strain), rapid response (approximately 160 ms), a wide sensing range (over 800%), and excellent cycle stability. This makes it a suitable candidate for wearable devices that monitor human activities, even in extremely cold temperatures (−30 °C). Additionally, these strain sensors can be used to develop sign language translators, achieving a recognition rate of up to 100% for complex sentences, bridging communication gaps between those unfamiliar with sign language and individuals with disabilities who rely on it. Thus, this design approach offers a novel method for fabricating highly efficient conductive hydrogels for flexible electronic devices, including electronic skin and flexible strain/stress sensors.

2 Materials and methods

2.1 Materials

We employed the following reagents in our experiments, adhering to the respective grade specifications: acrylic acid (AR grade) and ethylene glycol (AR grade) were sourced from Aladdin Reagent Company, ammonium persulfate (AR grade) from the same supplier, *N*,*N*-methylenebisacrylamide (99% electrophoresis grade) from Shanghai Macklin Biochemical Technology Co., Ltd., starch (food grade) from Shanghai Yuanye Biotechnology Co., Ltd., and a 10 mg mL^{-1} monolayer $Ti_3C_2T_x$ aqueous solution from Xinxi Technology Co., Ltd. These reagents were utilized without any additional purification steps.

2.2 Preparation of PAA/starch/MXene conductive organohydrogel

The process of starch gelatinization was carried out by dissolving starch in 3 mL of ethylene glycol while continuously stirring at 90 °C for 120 min, resulting in a homogeneous paste. Subsequently, 4 g of acrylic acid was added to the paste in various proportions, followed by the addition of *N*,*N*-methylenebisacrylamide (MBA) and deionized water with stirring for 15 min. An MXene aqueous solution was then gently mixed into the mixture using an ice-water bath with stirring for 10 minutes. Finally, ammonium persulfate was employed to initiate the formation of the organohydrogel, which was subsequently injected into a glass mold measuring 100 mm × 70 mm × 2 mm and heated at 60 °C for 8 h, resulting in the formation of a PAA/starch/MXene organohydrogel. The specific compositions of the organohydrogels are detailed in Table S1 of the ESI.†

2.3 Fabrication of the PAA/starch/MXene organohydrogel-based strain sensor

To showcase the strain-sensing capabilities of the PAA/starch/MXene organohydrogel, it was fashioned into a dumbbell-shaped specimen measuring 50 mm in length, 4 mm in width, and 2 mm in thickness. Subsequently, copper conductive tapes were meticulously employed to affix the organohydrogel onto the electrode interface of the LCR instrument, ensuring the robust transmission of signals.

2.4 Characterization

2.4.1 Characterization of structure and morphology. The Fourier Transform Infrared (FTIR) spectra of poly(acrylic acid) (PAA), PAA/starch, and PAA/starch/MXene organohydrogels were acquired using a ThermoFisher Nicolet iS10 spectrometer. Scanning Electron Microscope (SEM)

images of these organohydrogels were captured utilizing a TESCAN MIRA4 instrument. Raman spectra of starch, MXene, PAA, PAA/starch, and PAA/starch/MXene organohydrogels were recorded with a LABRAM HR EVOLUTION Raman spectrometer, employing 488 nm illumination. Prior to structural and morphological measurements, the organohydrogels underwent freeze-drying and fracturing in liquid nitrogen. Differential Scanning Calorimetry (DSC) spectra of the organohydrogels were determined using a TA DSC25 instrument, with a scanning speed of 5 °C min^{-1}, ranging from 40 °C to −70 °C in a nitrogen atmosphere.

2.4.2 Adhesion ability of the organohydrogel. The adhesion properties of the organohydrogel were thoroughly evaluated through both qualitative and quantitative methods. In the qualitative assessment, the organohydrogel was affixed to a diverse range of substrates, including stone, iron clip, copper sheet, glass, rubber, ceramic, silicone, and wood. To precisely quantify the adhesive strength of the organohydrogel to these various substrates, a lap shear test was conducted using a Lishi LE5000 universal material testing machine. This involved placing a rectangular piece of the organohydrogel with an adhesion area measuring 10 mm × 25 mm between two symmetrical substrates. Subsequently, the setup was clamped and subjected to a constant stretching speed of 5 mm min^{-1} until the organohydrogel and substrates separated. For the lap shear test, we selected substrates that included polytetrafluoroethylene (PTFE), pigskin, glass, iron sheet, and copper sheet. To minimize energy dissipation during stretching, the pigskin was carefully cut into a 10 mm × 25 mm rectangle and securely affixed to a glass plate using super glue. The adhesive strength of the organohydrogel was quantitatively determined by calculating the ratio of the maximum adhesion force to the area of adhesion overlap.

2.4.3 Mechanical and sensing performance of the organohydrogel-based sensor. A microcomputer-controlled Lishi LE5000 electronic universal testing machine was used to measure the tensile and compression properties of organohydrogels. The stretching and compressing speed were set at 50 mm min^{-1} and 2 mm min^{-1}, respectively. For uniaxial tensile tests, the samples were cut into a dumbbell shape with a length of 50 mm, width of 4 mm, and thickness of 2 mm. For compression tests, the samples were cut into a cylinder shape with a diameter of 22 mm and a height of 20 mm. Young's modulus was calculated from the strain–stress curves in the 0–10% strain range. The average results of five experiments were used to determine the tensile stress, fracture strain, Young's modulus, and toughness.

The fracture strain ε is calculated by the equation of $\varepsilon = \frac{L-L_0}{L_0} \times 100\%$, where L_0 and L are the initial and fractured lengths of the organohydrogel, respectively.[53] The rupture stress σ is determined by the equation of $\sigma = \frac{F}{A_0}$, where F (N) is the applied force and A_0 (mm^2) is the cross-sectional area of the sample. The sensing performance and demonstrations of the sensors were evaluated using a testing system that included a Lishi LE5000 universal electronic test machine, a computer, and an inductance, capacitance, and resistance (LCR) measurement instrument (IM3536, HIOKI, Japan). The gauge factor[54] of the strain sensor is defined by the equation of $GF = \frac{R-R_0}{R_0}/\varepsilon$, where R_0 and R represent the resistances of organohydrogels in the original state and stretching state, respectively, and ε was the strain of the sensor.

3 Results and discussion

The formation mechanism of the PAA/starch/MXene organohydrogel is depicted in Fig. 1a. Initially, starch is gelatinized in a mixed solution containing ethylene glycol. During this process, the crystalline regions within the starch particles gradually transition from a tightly packed state to a more relaxed state, leading to the rupture of starch particles and the dispersion of starch molecules into the aqueous phase. This dispersion not only involves the formation of hydrogen bonds between these molecular chains but also their interweaving, resulting in an enhancement of the interaction forces between the chains and the creation of a denser network structure (Fig. 1b and c). Subsequently, AA, MBA, MXene, and APS are successively dispersed in the gelatinized starch solution through continuous ultrasonication, followed by the addition of APS to the mixed solution and heating for polymerization. Finally, the introduction of highly dispersible MXene nanosheets, which can form hydrogen bonds with the gelatinized starch, significantly improves the even dispersion of starch within the hydrogel system. Furthermore, the physical interactions between PAA, starch, MXene, and ethylene glycol contribute to the construction of a stable and uniform three-dimensional network structure (Fig. 1d). The network structure of the PAA/starch/MXene organohydrogel has undergone transformation due to increased hydrogen bonding interactions, resulting in enhanced mechanical properties, including remarkable stretchability of over 400% strain without visible damage when knotted and twisted (Fig. 1e), as well as excellent deformability and recoverability when compressed (Fig. S1†). Elemental mapping images of the organohydrogel reveal even distribution of C, O, F, and Ti elements, confirming effective MXene dispersion and the formation of a uniform conductive network (Fig. 1f).

FTIR and Raman measurements were conducted to analyze the composition of PAA, PAA/starch, and PAA/starch/MXene organohydrogels. FTIR analysis indicated a shift in the peak at 3370 cm^{-1} associated with the –OH group to a lower wavenumber and broadening upon the addition of starch and MXene, suggesting the formation of additional hydrogen bonds within the organohydrogel[55] (Fig. 1g). Furthermore, Raman spectroscopy identified characteristic peaks from both starch (477 cm^{-1}, 863 cm^{-1}, 939 cm^{-1}, and 1127 cm^{-1}) and PAA (863 cm^{-1}, 1042 cm^{-1}, and 1087 cm^{-1}) in PAA/starch and PAA/starch/MXene organohydrogels, along

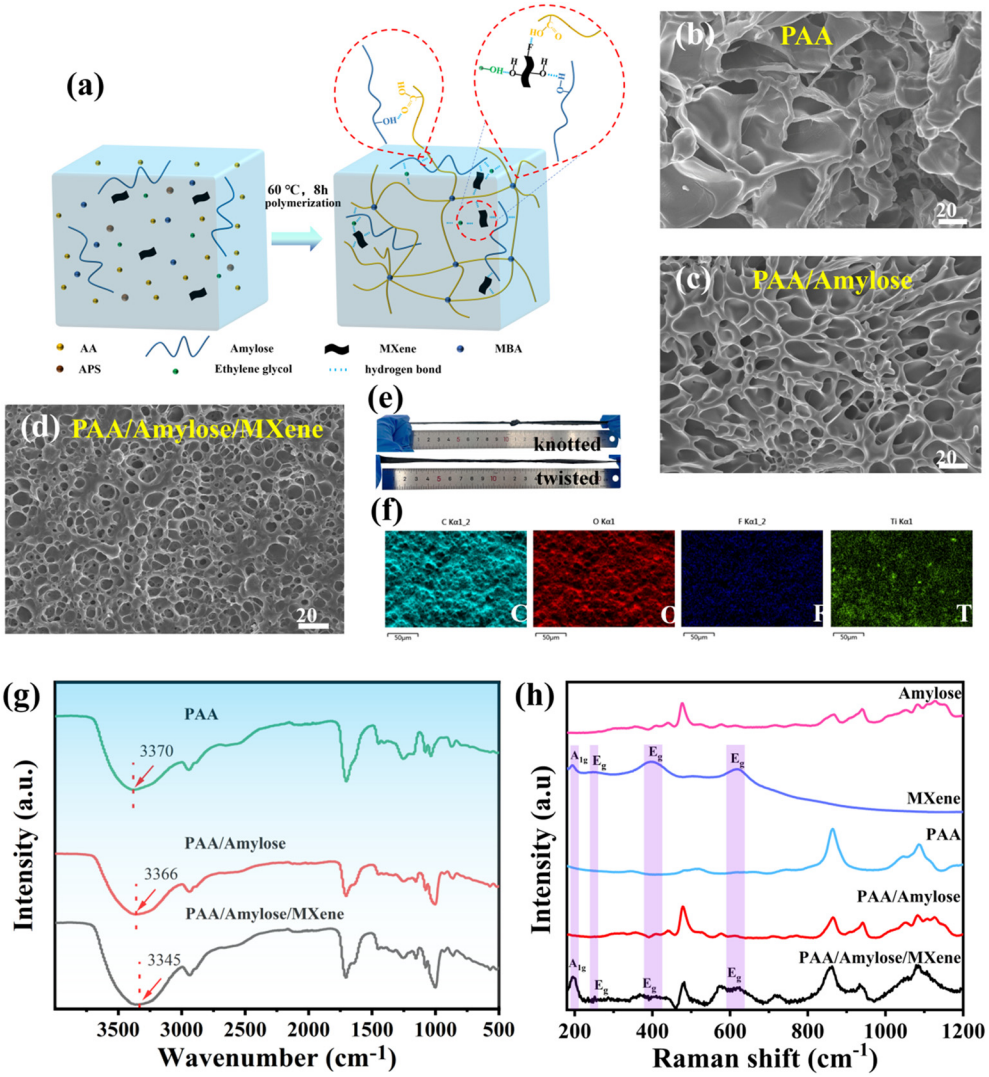

Fig. 1 Fabrication and structural characterization of the organohydrogels. (a) Schematic of the synthesis process for PAA/starch/MXene organohydrogel; SEM images of (b) PAA, (c) PAA/starch and (d) PAA/starch/MXene organohydrogels; (e) stretchability of the PAA/starch/MXene organohydrogel with knotted and twisted states; (f) elemental mapping images of C, O, F, and Ti elements in the PAA/starch/MXene organohydrogel; (g) FTIR spectra and (h) Raman spectra of the organohydrogels.

with the distinctive A_{1g} and E_g peaks of MXene nanosheets in the PAA/starch/MXene organohydrogels[56,57] (Fig. 1h). These findings confirm the successful integration of starch and MXene into the organohydrogel, and the formation of hydrogen bonds among the components.

The tensile and compressive properties of PAA, PAA/starch, and PAA/starch/MXene organohydrogels were compared in Fig. 2a and S2,† respectively. The results revealed a progressive increase in fracture strain and fracture stress from PAA to PAA/starch, and further to PAA/starch/MXene, illustrating the effective enhancement of mechanical strength through the incorporation of starch and MXene. Moreover, the fracture energy and Young's modulus of the PAA/starch/MXene organohydrogel significantly surpassed those of the PAA and PAA/starch organohydrogels, measuring 2.40 MJ m^{-3} and 211 kPa, compared to 0.24 MJ m^{-3} and 27.64 kPa, and 0.71 MJ m^{-3} and 61.55 kPa, respectively (Fig. 2b and c).

Fig. S2† demonstrated the organohydrogels' ability to withstand compression deformation up to 90%. Notably, the PAA/starch/MXene organohydrogel exhibited the highest compressive stress, indicating the reinforcing roles of starch and MXene. This improvement in mechanical properties is likely attributed to the formation of a homogeneous and densely cross-linked network, facilitated by augmented hydrogen bonding. We also explored the impact of starch on the mechanical properties of the organohydrogels in Fig. 2d, revealing that the fracture strain of the PAA/starch organohydrogel initially increased and then decreased with increasing starch content, while fracture strength, fracture energy, and Young's modulus were all enhanced. Their peak values were achieved when the starch/AA ratio was 3 : 7 (Fig. 2e and f). This is likely due to the increased cross-link density, resulting in more hydrogen bonds and increased energy dissipation during stretching, ultimately improving

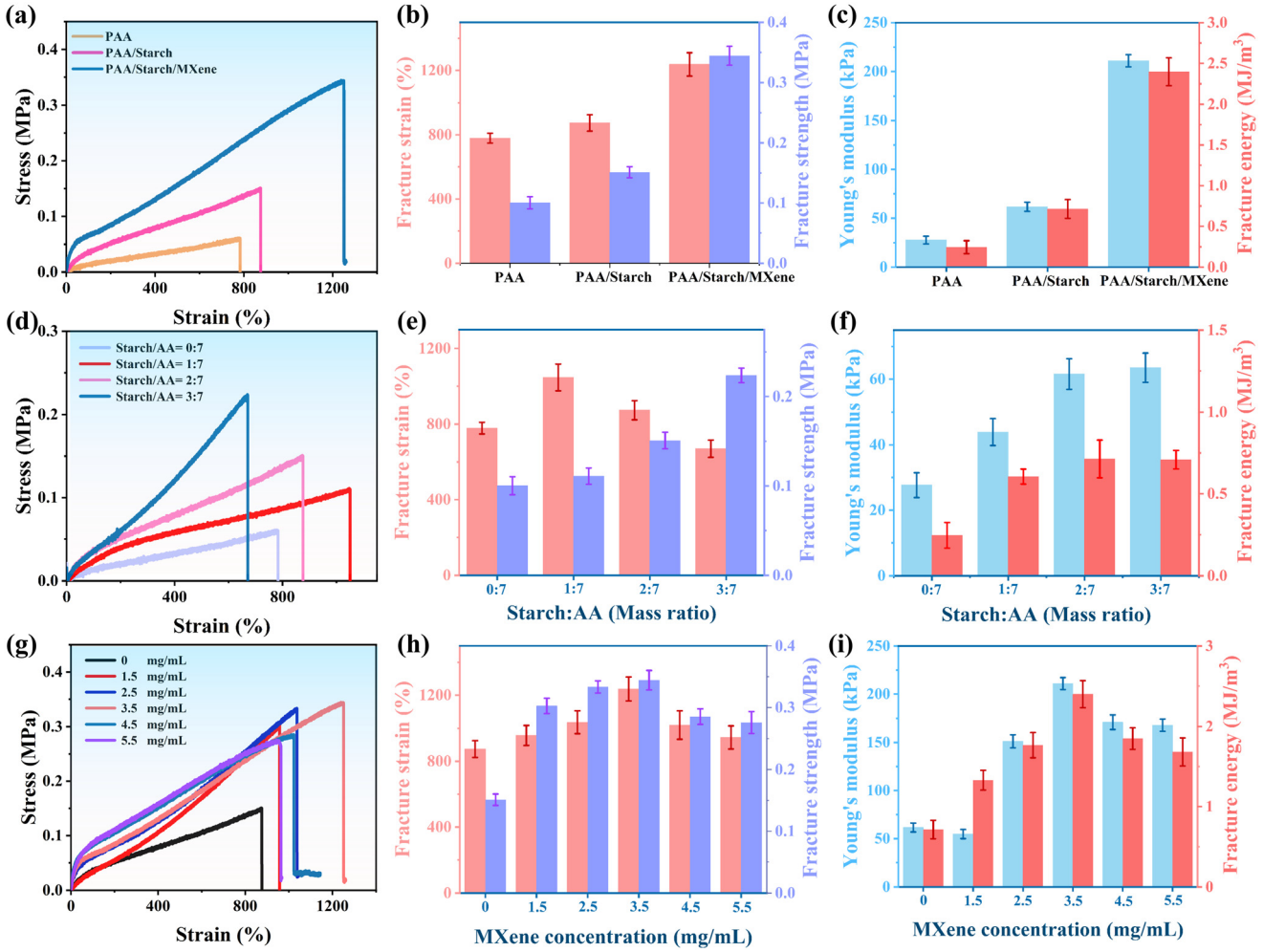

Fig. 2 Effects of components, the mass ratio of starch to AA, and MXene concentration on the mechanical properties of the hydrogels. (a) Typical tensile stress–strain curves of PAA, PAA/starch, and PAA/starch/MXene organohydrogels; (d) PAA/starch organohydrogel with different contents of starch; (g) PAA/starch/MXene organohydrogels with different concentrations of MXene; calculated (b, e and h) fracture strain and fracture strength and (c, f and i) Young's modulus and fracture energy of the organohydrogels.

the mechanical properties of the organohydrogels. Considering the mechanical properties, we selected PAA/starch with a starch/AA ratio of 2 : 7 for further modification. An excessive concentration of starch can lead to high viscosity, which can impede the formation of a uniform network structure and reduce fracture strain. The typical tensile stress–strain curve of PAA/starch/MXene organohydrogel with different concentrations of MXene is presented in Fig. 2g, clearly demonstrating that the mechanical properties of the organohydrogel improve and then decline with increasing MXene concentration (Fig. 2h and i).

Fig. S3a† reveals the dynamic thermal-mechanical properties of the hydrogels under varying angular frequencies. The figure shows that adding starch and MXene nanosheets markedly increases the storage modulus, significantly enhancing the composite hydrogel's elasticity. Throughout the frequency sweep, the storage modulus (G') remains higher than the loss modulus (G''), indicating a predominantly elastic, cross-linked network structure within the hydrogels. The inclusion of nanoscale and microscale particles generally raises the gel's viscosity and elasticity, thereby boosting the loss modulus of the composite gel. Our investigation into the temperature effects on the PAA/starch/MXene organohydrogel's storage (G') and loss moduli (G'') reveals that at lower temperatures (−30 °C), the hydrogel displays a high storage modulus and a low loss modulus. This implies strong intermolecular interactions at the crosslinking points, leading to a stable, elastic gel network with minimal energy dissipation. As the temperature increases, the molecular chains in the hydrogel become more active, reducing intermolecular forces. Consequently, the storage modulus decreases, reflecting a reduction in gel elasticity. However, the loss modulus remains relatively constant, suggesting stable energy dissipation within the −30 to 25 °C range. Thus, the Dynamic Mechanical Analysis (DMA) results further substantiate the strong, multifaceted interactions between MXene, PAA, and starch, significantly reinforcing the material's rigid network structure.

The incorporation of MXene into the PAA/starch organohydrogel at a concentration of 3.5 mg mL^{-1} has demonstrated a significant improvement in its mechanical properties. This enhancement is evident through the increased fracture strain, fracture stress, Young's modulus, and fracture energy values. This improvement can be attributed to the presence of –OH, –F, and –O functional groups on the MXene surface, which facilitate non-covalent interactions with other components. However, it is essential to note that an excessive amount of MXene can lead to an uneven distribution within the network, resulting in a reduction in the organohydrogel's mechanical strength. When considering the application of this organohydrogel in strain sensors, fatigue resistance becomes a crucial factor. This resistance can be evaluated through tensile loading-unloading tests. Fig. S4a–c† illustrates the loading-unloading curves of PAA, PAA/starch, and PAA/starch/MXene organohydrogels at strains ranging from 100% to 300%. These curves clearly indicate an increase in the hysteresis loop areas of all organohydrogels as the strain increases, demonstrating their effective energy dissipation capacity.

Furthermore, we examined the loading-unloading behavior of these organohydrogels at a consistent strain of 200% (Fig. S4d†) and calculated the corresponding dissipated energy (Fig. S4e†). Notably, the PAA/starch/MXene organohydrogel exhibited the highest dissipated energy compared to the PAA and PAA/starch organohydrogels. This improvement is attributed to the abundant hydrogen bonding and electrostatic interactions between MXene, starch, and PAA polymer chains. Additionally, we conducted successive cyclic tensile loading-unloading experiments on the organohydrogels with a maximum tensile strain of 200% (Fig. S4f–h†). After 10 cycles of loading and unloading, the PAA/starch/MXene organohydrogel exhibited the least amount of residual strain and its hysteresis loop nearly coincided, surpassing the performance of the PAA and PAA/starch organohydrogels. This implies that the integration of starch and MXene into the organohydrogel boosts physical interactions, thereby strengthening its resistance to fatigue. As a result, the PAA/starch/MXene organohydrogel is a promising material for the fabrication of hydrogel-based sensors for long-term applications.

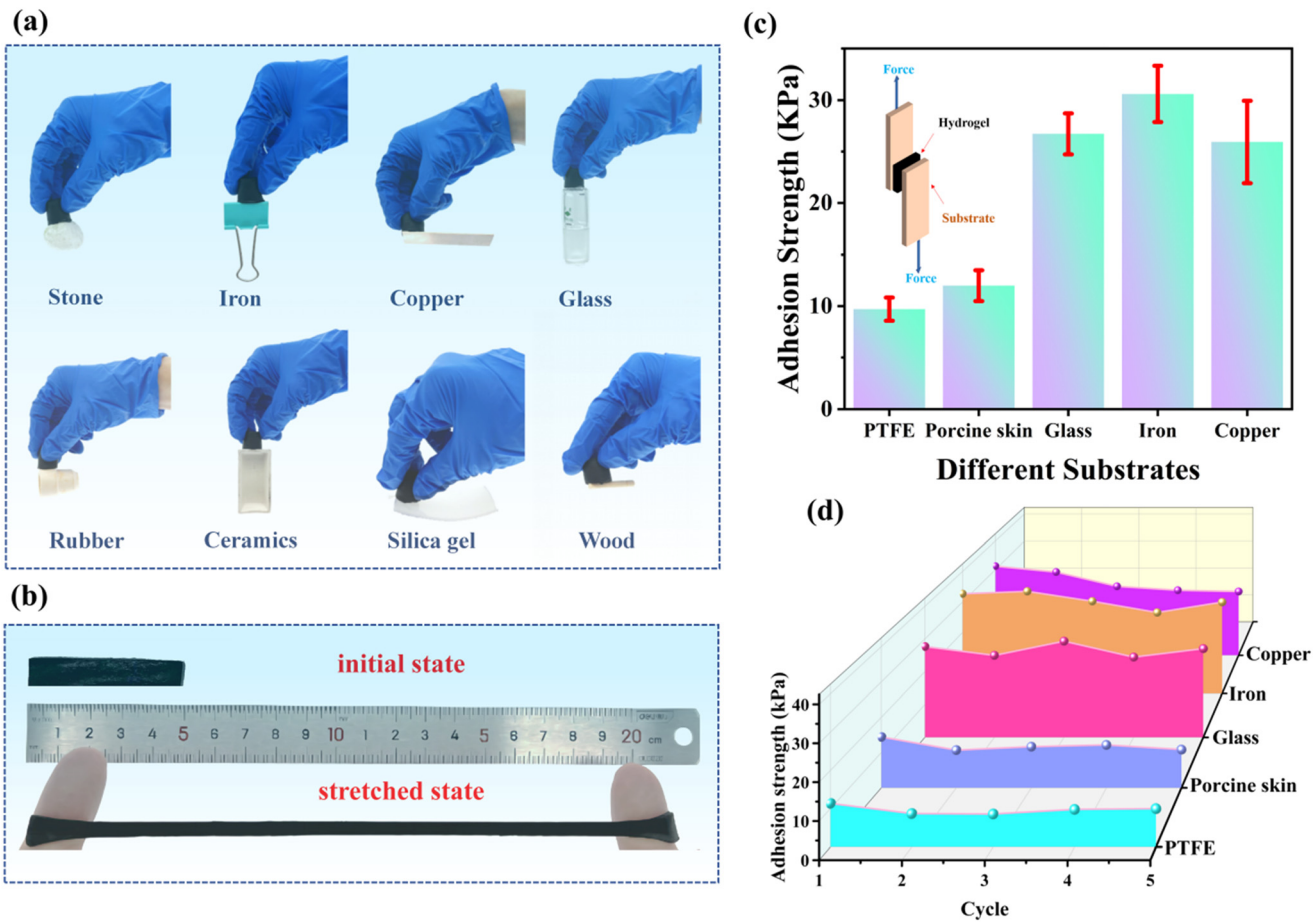

Fig. 3 Adhesion ability of the PAA/starch/MXene organohydrogel. (a) Adhesive abilities to various materials; (b) adhesion to the fingers when it was stretched to 400% strain deformation; (c) adhesion strength to different substrates in air determined by tensile adhesion tests; (d) repeatable adhesion behaviors to different substrates for five adhesion-peeling cycles.

The utilization of strain sensors in wearable devices often requires recalibration due to uncertain initial pressure. Achieving accurate detection of human motion and physiological signals is crucial, and an adhesive sensor that can directly adhere to the skin offers distinct advantages. The proposed PAA/starch/MXene organohydrogel, with its numerous functional groups such as –OH, –O, –F, and COO–, exhibits versatile adhesion capabilities to a wide range of materials, as demonstrated in Fig. 3a. Importantly, it adheres firmly to human skin without any pre-treatment, withstanding stretching cycles of up to 400% strain when applied to fingers (Fig. 3b). To assess the adhesive strength of the PAA/starch/MXene organohydrogel on different material surfaces (*e.g.*, PTFE, pigskin, glass, iron, and copper), we conducted cyclic lap shear experiments in tensile mode, as depicted in Fig. 3c. The results reveal that the adhesive strength of the organohydrogel is highest on iron surfaces (9.70 kPa, 11.98 kPa, 26.72 kPa, 30.59 kPa, and 25.93 kPa for PTFE, pigskin, glass, iron, and copper, respectively). This superior adhesion can be attributed to the strong hydrogen and ionic coordination bonding between the organohydrogel and the iron substrate. Moreover, the PAA/

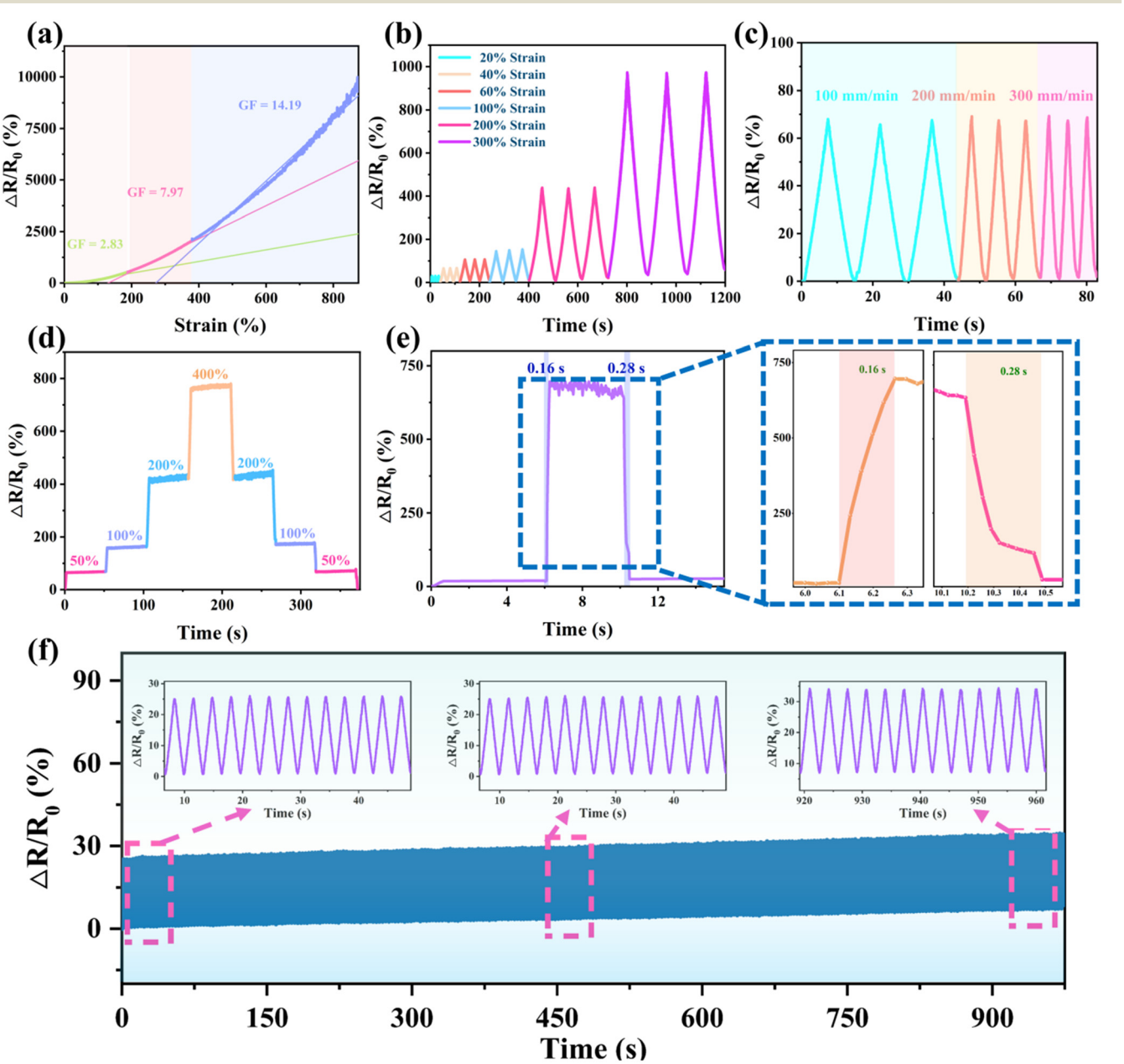

Fig. 4 Sensing performance of the PAA/starch/MXene organohydrogel-based strain sensor. (a) Resistance change-strain curves in 0–880% strain range; (b) resistance changes at 20, 40, 60, 100, 200, and 300% strain, respectively; (c) response to different stretching speeds of 100, 200, and 300 mm min^{-1} at 50% strain (d) and step increased and decreased strains of 50, 100, 200, and 400%; (e) response and recovery time of the instantaneous tensile deformation; (f) long-term stability at 30% strain for 300 cycles; the inset is partially magnified curves for intermediate cycle stage.

starch/MXene organohydrogel exhibits reversible adhesive properties on different substrates, with its adhesive strength remaining nearly unchanged even after five cycles of adhesion-peeling tests (Fig. 3d and S5†).

Due to its outstanding stretchability, adhesion, fatigue resistance, and remarkable electronic conductivity, the PAA/starch/MXene organohydrogel is poised for utilization as a resistive sensor. Fig. 4a illustrates that the organohydrogel-based sensor exhibits three linear intervals of relative resistance change rates: 0–185%, 185–380%, and 380–880%, with corresponding sensor sensitivities of 2.83, 7.97, and 14.19, respectively. As strain increases, the gap between MXene nanosheets widens, influencing the electron transport path and consequently increasing the organohydrogel's resistance. The robustness of the organohydrogel network ensures a constant conductive network even under an 880% strain. In Fig. 4b, it is evident that the PAA/starch/MXene organohydrogel-based device maintains consistent and reversible signals during successive stretching–releasing cycles at both small (20%, 40%, 60%) and large (100%, 200%, 300%) strain, affirming its response stability.

Three consecutive stretches at speeds of 100, 200, and 300 mm min^{-1}, each at a 50% strain, were applied to the sensor, with no observable change in the amplitude of electrical signal (Fig. 4c). Moreover, subjecting the stretchable sensor to incremental tensile strains from 0% to 400% resulted in a symmetrical step response, underscoring its exceptional recoverability under varying strains (Fig. 4d). The response and recovery time of the sensor during typical transient tensile deformation were determined to be 160 ms and 280 ms, respectively, highlighting its rapid response characteristics (Fig. 4e). Furthermore, long-term stability assessment of the hydrogel-based sensor involved cyclic stretching and releasing at a 30% strain for 300 cycles. The results revealed a consistent amplitude of resistance change without any signal attenuation or delay, affirming its potential as a strain sensor with both sensitivity and stable response (Fig. 4f). We have included a comprehensive performance comparison between our PAA/starch/MXene organohydrogel and reported starch-based hydrogel strain sensors in Table S2.† In comparison to other similar hydrogels, the starch-based sensor we designed demonstrates a superior performance across various criteria, such as high sensitivity and outstanding mechanical performance.

We demonstrate the use of PAA/starch/MXene organohydrogel-based strain sensors as wearable devices with remarkable self-adhesive properties. These sensors are capable of monitoring the continuous flexing and unflexing of finger joints in real-time, as depicted in Fig. 5a. When the finger bends, the sensor exhibits an increase in relative resistance, which promptly returns to its original state upon finger straightening, underscoring its rapid response and impressive reversibility, as illustrated in Fig. 5b. Additionally, we affixed the sensor to elbow and wrist joints to detect the motion of different joints, as exemplified in Fig. 5c and d. Notably, when the device is applied to smaller joints like the

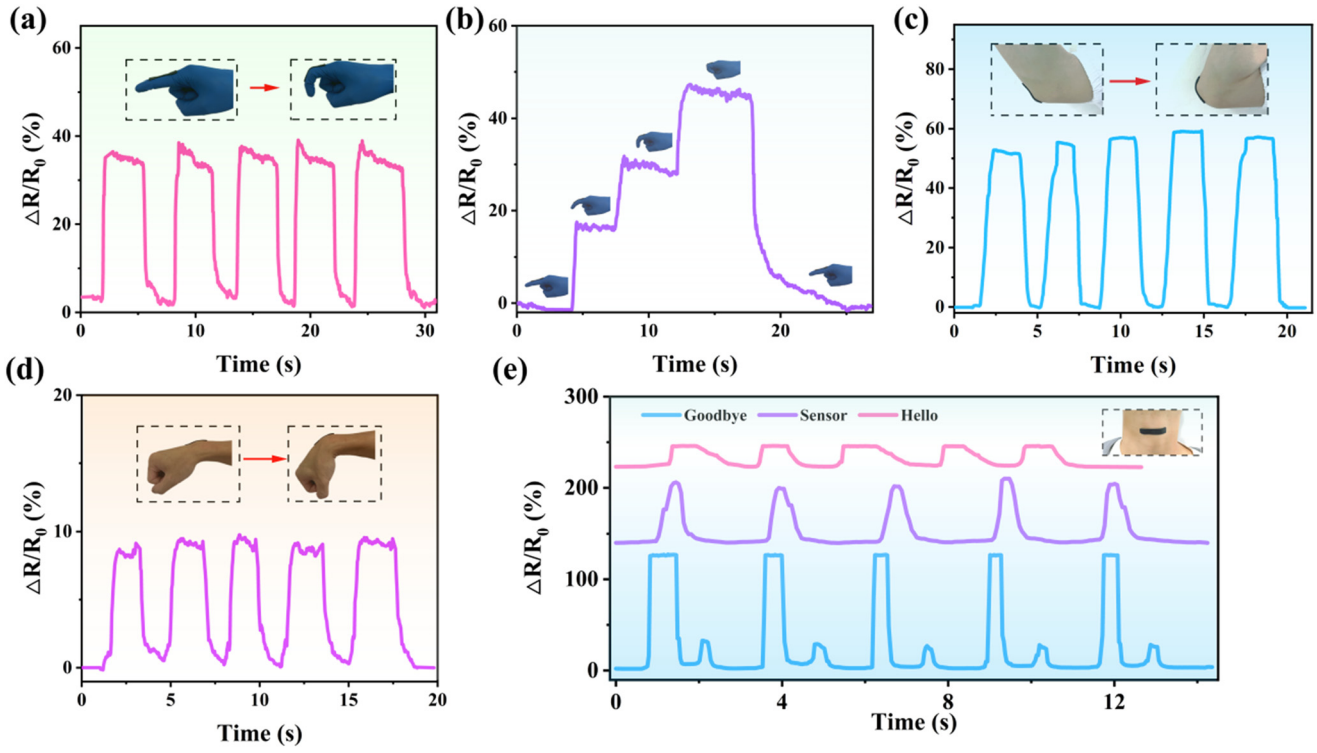

Fig. 5 Demonstration of PAA/starch/MXene organohydrogel-based strain sensor in human motion monitoring. (a) Real-time relative resistance changes for the detection of repeated finger bending, (b) finger bending at different angles, (c) elbow bending, (d) wrist bending, (e) speaking.

wrist and finger, minor signal disturbances occur when the body part is in a straight position. This phenomenon is attributed to the secure adhesion between the device and the skin, resulting in fluctuations in electrical signals primarily due to skin fold tension on the device. Furthermore, the organohydrogel-based sensor proved effective in monitoring subtle muscle motions during activities such as speaking and swallowing, as depicted in Fig. 5e and S6.† When attached to the throat, the device captured distinctive waveforms when various words like "Goodbye", "Sensor", and "Hello" were spoken. Furthermore, repeating the same word yielded consistent waveforms, highlighting the excellent signal repeatability of the strain sensor.

Intelligent sensing systems have the capability to acquire, analyze, recognize, and adapt to their environment in real-time. The PAA/starch/MXene organohydrogel-based strain sensors are poised to find extensive applications in these systems due to their exceptional self-adhesion and close skin contact properties. These qualities can enhance the signal-to-noise ratio of collected data and the effectiveness of machine learning algorithms. In this study, we employ organohydrogel-based strain sensors for sign language recognition, thereby facilitating communication with sign language users. Five sensors were directly attached to the thumb, index finger, middle finger, ring finger, and little finger, enabling the expression of complex sentences using the 26 English letters of international sign language (Fig. S7†). As depicted in Fig. 6a and b, we successfully translated five sentences, including "Wuyi University", "What time is it now", "What is your name", "Where are you from", and "How much is this" from sign language into electronic signals. To accomplish this, we utilized the *K*-nearest neighbors (KNN) algorithm for training and classification across the five categories. Each sensor collected ten sets of data, with seven sets designated for training and the remaining three for testing. The collected data were subsequently segmented into 100 groups of feature values, resulting in a total of 500 feature values within the time domain. These data points were organized into lists, converted into numerical values or integers, and then transformed into a NumPy array to enable efficient data processing. The confusion matrix presented in Fig. 6c revealed that the recognition rate for the five typical sentences reached 100%, underscoring the promising potential of these fabricated sensors for future applications in intelligent sensing systems.

Investigations have revealed that under sub-zero temperatures, most conductive hydrogels tend to exhibit reduced flexibility and diminished conductivity. To assess the suitability of the PAA/starch/MXene organohydrogel under extreme conditions, we conducted DSC analysis over a temperature range spanning from −70 to 40 °C, as depicted in Fig. 7a. We observed an exothermic peak at −35.35 °C,

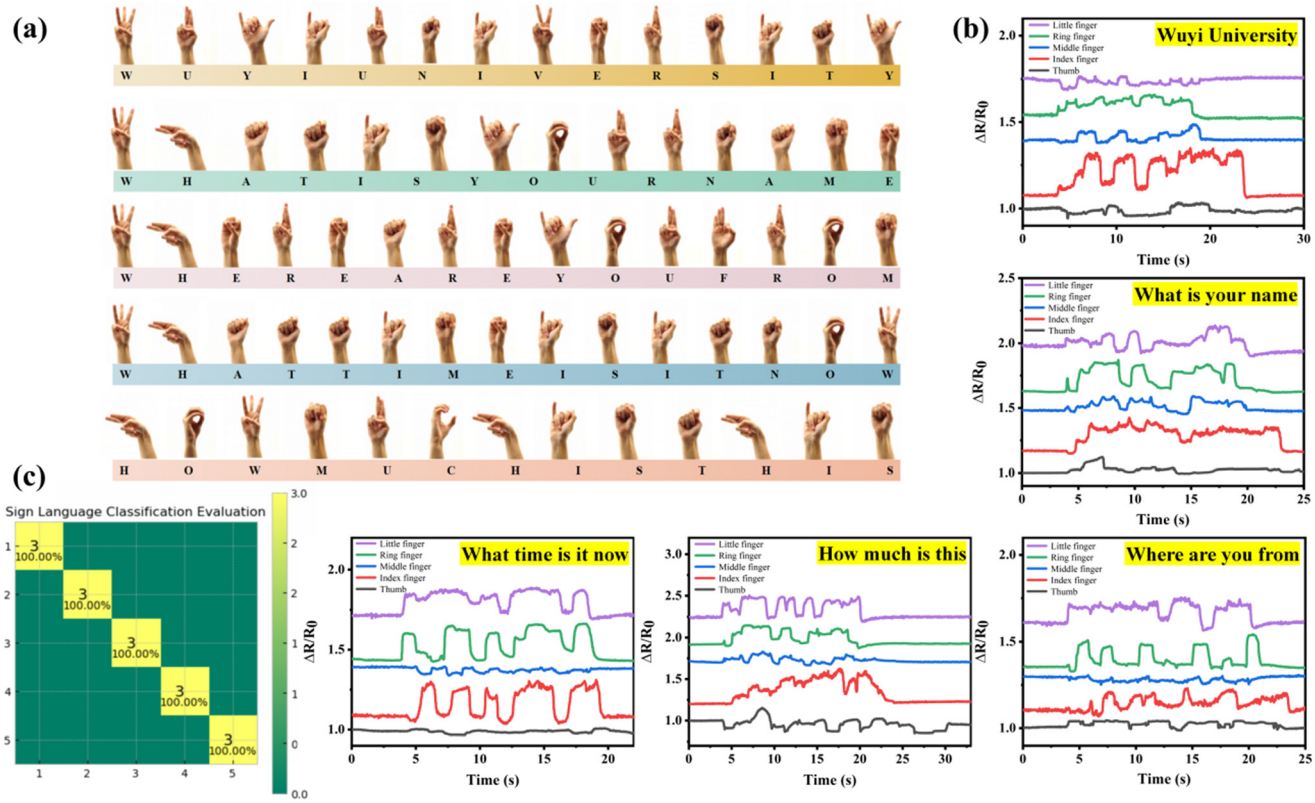

Fig. 6 Sign language recognition of the strain sensors. (a) Sign language corresponding to five sentences; (b) resistance change curves of five sensors in response to different sentences; (c) confusion matrix to sign language recognition derived from machine learning with 10 sets of data for each category.

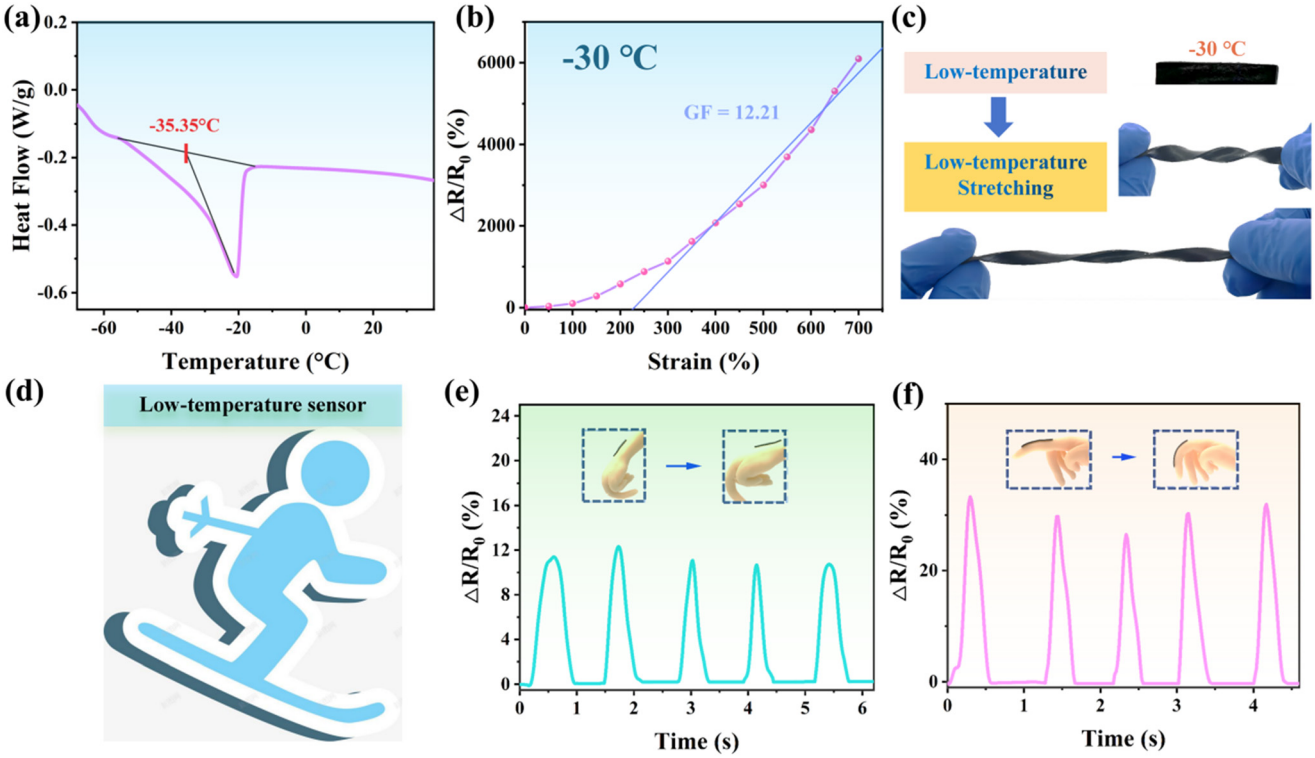

Fig. 7 Anti-freezing property of the PAM organohydrogel-based strain sensor. (a) DSC curve in the temperature range of −70–40 °C; (b) resistance change-strain curve at −30 °C; (c) photos of stretching sensor with and without EG at −30 °C and 20 °C; (d) application scenario in low-temperature environment; response of the sensor attached to wrist (e) and finger (f) of a silicon at −30 °C to the repeated bending.

aligning with the freezing point of the PAA/starch/MXene organohydrogel. Moreover, the organohydrogel exhibited resilience against deformations such as twisting and stretching at −30 °C, illustrating its anti-freezing properties (Fig. 7b and c). This remarkable anti-freeze capability can be attributed to the incorporation of ethylene glycol as a co-solvent in the water, which fosters robust hydrogen bonding to counteract free water within the system and impedes ice lattice formation at low temperatures. This enhanced anti-freeze performance positions the organohydrogel as a viable candidate for applications in winter sports, such as skiing (Fig. 7d). We also observed that electrical signals generated by sensors affixed to the wrist and fingers of a silicone hand remained stable during repeated joint bending at −30 °C (Fig. 7e and f). The consistent cyclic waveforms affirm the PAA/starch/MXene organohydrogel's ability to endure rapid mechanical distortions while maintaining its electrical conductivity, even in frigid conditions.

Furthermore, we conducted an investigation into the anti-drying properties of the PAA/starch/MXene organohydrogel in comparison to a control group that lacked ethylene glycol (Fig. S8†). Both sets of hydrogels were exposed to an environment with room temperature and 50% relative humidity (RH) for a duration of 7 days, and their ability to resist drying was meticulously analyzed and compared. To quantify this, we recorded the initial weight (W_0) and the weight after the specified period (W_t) for each hydrogel sample. The anti-drying performance of the hydrogel was assessed using the ratio W_t/W_0. Upon a thorough examination of the results, it becomes evident that, after 7 days of exposure, the hydrogel without ethylene glycol experienced a significant loss of moisture, with its weight decreasing to approximately 42.39% of the initial weight due to severe dehydration. In stark contrast, our PAA/starch/MXene organohydrogel displayed remarkable water retention capabilities, retaining approximately 70.0% of its initial weight after the same 7 day period. This stark contrast in behavior can be attributed to the presence of ethylene glycol, which is non-volatile, possesses a low saturation vapor pressure, and exhibits hygroscopic properties. Furthermore, the formation of strong hydrogen bonds between ethylene glycol molecules and water molecules effectively hinders the evaporation of water from the organohydrogel.

A pressure sensor was employed to assess the response of PAA/starch/MXene organohydrogels to compression. Fig. 8a illustrates the fluctuation in sensor resistance when compressing and releasing the columnar organohydrogel with a finger. This phenomenon arises from the reduction in the gap between the MXene nanosheets within the organohydrogel structure. Analysis of a loading-unloading cycle allowed us to determine the response time and recovery time of the pressure sensor, which were found to be 150 ms and 160 ms, respectively (Fig. 8b), indicative of its rapid response characteristics. When subjecting the device to vertical pressures ranging from 0 to 150 kPa, the resistance change rate exhibits three linear intervals (Fig. 8c). This

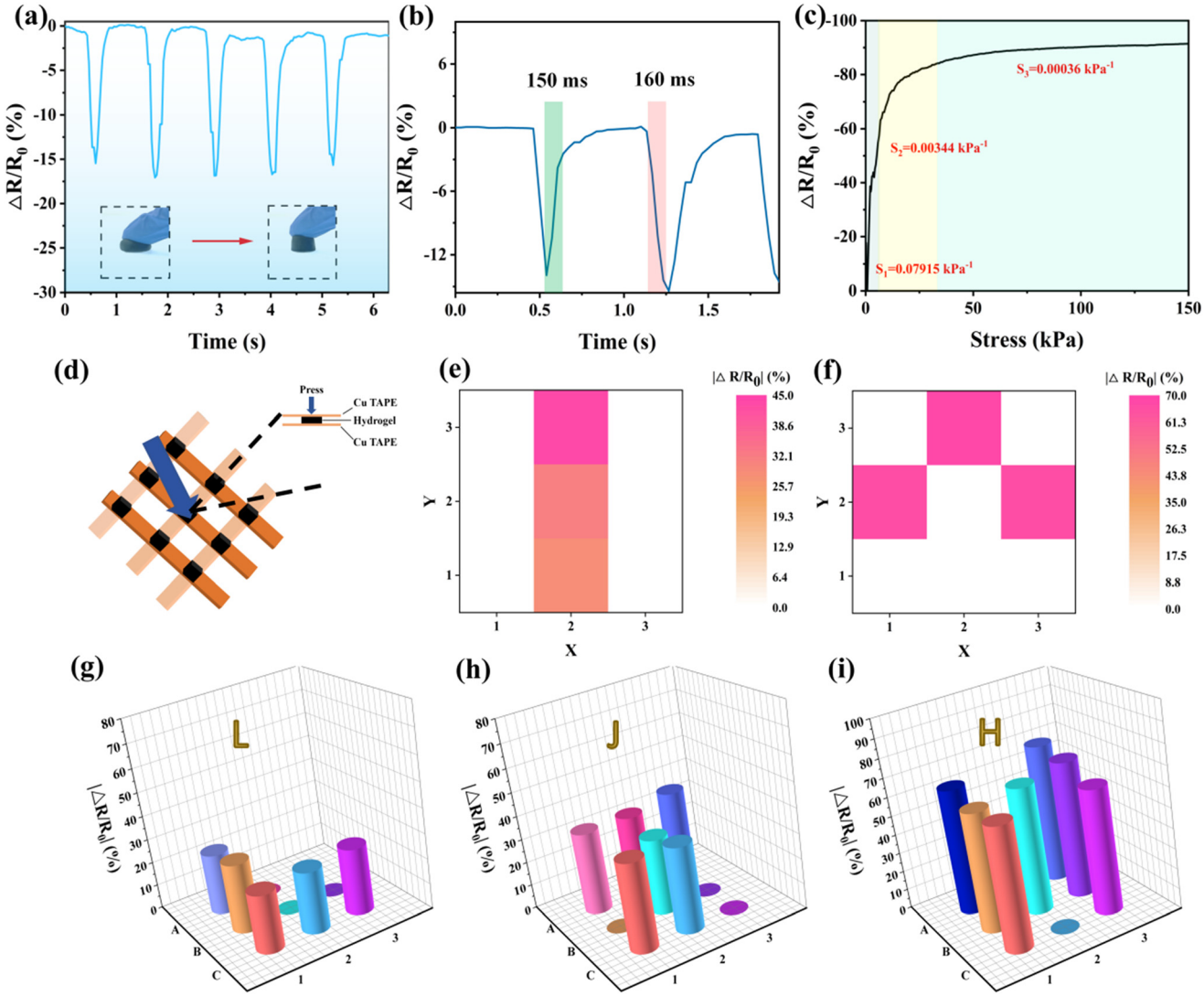

Fig. 8 Demonstration of the PAA/starch/MXene organohydrogel-based pressure sensor. (a) Response to compressing and releasing; (b) response and recovery time; (c) relative resistance changes as a function of pressure; (d) sketch of 3 × 3 array of pressure sensors; 2D pressure distributions of static loading (e and f); 3D pressure distributions of writing the letters 'L' (g), 'J' (h), and 'H' (i).

variation in resistance highlights the device's heightened sensitivity to lower pressures, as the organohydrogel's deformation reaches saturation due to its low Young's modulus. Consequently, the gaps between the MXene nanosheets can no longer be further reduced, resulting in decreased sensitivity to larger external forces. To facilitate pressure distribution detection, we constructed an array comprising nine organohydrogel cylinders, copper conductive tape, and PET film, as depicted in Fig. 8d. By plotting the resistance changes for each sensor, we can generate two-dimensional mapping images of the pressure distribution, as demonstrated in Fig. 8e and f. These maps provide insights into the location and magnitude of the load when applying different weights to various sensors. Furthermore, tracing the letters "L", "J", and "H" on the array with a finger enables the creation of a three-dimensional mapping image of pressure distribution, as illustrated in Fig. 8g–i. These images vividly depict the shapes of the letters and the intensity of the applied writing force. This underscores the potential of the hydrogel-based sensor array as a platform for developing smart artificial electronic skins capable of detecting tactile signals and mapping spatial pressure distribution. Furthermore, future endeavors should be directed towards the commercialization, downsizing, and lightweight design of wearable sensors through large-scale manufacturing processes.

4 Conclusions

The PAA/starch/MXene conductive organohydrogel was successfully synthesized using a hydrogen bond strengthening strategy, resulting in a material characterized by robustness, self-adhesion, frost resistance, and fatigue resistance. The addition of starch and MXene significantly

enhanced the mechanical properties of the organohydrogel through increased physical interactions among its components. Moreover, the presence of various functional groups (–OH, –O, –F, and COO–) endowed the organohydrogel with the ability to adhere to diverse surfaces, rendering it suitable for applications in wearable sensors. As a result, the strain sensor based on this organohydrogel exhibited an extensive detection range (up to 880% strain), high sensitivity (GF = 14.19), inherent self-adhesion, remarkable stability, and resistance to frost (−30 °C). This organohydrogel-based sensor can be securely affixed to human skin, enabling accurate detection of joint and muscle movements, sign language interpretation, as well as measurement of stress intensity and spatial distribution. Therefore, PAA/starch/MXene conductive organohydrogels hold significant promise for the development of multifunctional hydrogel-based strain sensors.

Data availability

Data will be made available on request.

Conflicts of interest

The authors declare no competing interests.

Acknowledgements

This work was supported by the Natural Science Foundation of Guangdong Province (2021A1515010691); College Innovation Team Project of Guangdong Province (2021KCXTD042); Wuyi University-Hong Kong-Macau Joint Research and Development Fund (2019WGALH06, 2022WGALH04); Science Foundation for High-level Talents of Wuyi University (2020AL003); Jiangmen Basic and Theoretical Scientific Research Science and Technology Plan Project (2020JC01022); Key Project of Jiangmen Basic and Applied Basic Research (202103010370000739 2).

References

1 A. Chortos, J. Liu and Z. Bao, *Nat. Mater.*, 2016, **15**, 937–950.
2 J. Shin, B. Jeong, J. Kim, V. B. Nam, Y. Yoon, J. Jung, S. Hong, H. Lee, H. Eom, J. Yeo, J. Choi, D. Lee and S. H. Ko, *Adv. Mater.*, 2020, **32**, 1905527.
3 H. Wang, S. Li, Y. Wang, H. Wang, X. Shen, M. Zhang, H. Lu, M. He and Y. Zhang, *Adv. Mater.*, 2020, **32**, 1908214.
4 K. Xu, Y. Lu, S. Honda, T. Arie, S. Akita and K. Takei, *J. Mater. Chem. C*, 2019, **7**, 9609–9617.
5 S. Han, C. Liu, X. Lin, J. Zheng, J. Wu and C. Liu, *ACS Appl. Polym. Mater.*, 2020, **2**, 996–1005.
6 J. Wu, W. Huang, Z. Wu, X. Yang, A. G. P. Kottapalli, X. Xie, Y. Zhou and K. Tao, *ACS Mater. Lett.*, 2022, **4**, 1616–1629.
7 K. Zhai, H. Wang, Q. Ding, Z. Wu, M. Ding, K. Tao, B. R. Yang, X. Xie, C. Li and J. Wu, *Adv. Sci.*, 2023, **10**, 2205632.
8 S. Han, C. Liu, Z. Huang, J. Zheng, H. Xu, S. Chu, J. Wu and C. Liu, *Adv. Mater. Technol.*, 2019, **4**, 1800640.
9 S. Han, Q. Wan, K. Zhou, A. Yan, Z. Lin, B. Shu and C. Liu, *ACS Appl. Nano Mater.*, 2021, **4**, 8273–8281.
10 Z. Chen, J. Liu, Y. Chen, X. Zheng, H. Liu and H. Li, *ACS Appl. Mater. Interfaces*, 2021, **13**, 1353–1366.
11 L. Dai, M. Ma, J. Xu, C. Si, X. Wang, Z. Liu and Y. Ni, *Chem. Mater.*, 2020, **32**, 4324–4330.
12 C. Li, *RSC Adv.*, 2021, **11**, 33835–33848.
13 J. Liang, J. He, Y. Xin, W. Gao, G. Zeng and X. He, *Macromol. Mater. Eng.*, 2022, **308**, 2200519.
14 L. Zhang, J. Wang, S. Wang, L. Wang and M. Wu, *J. Mater. Chem. C*, 2022, **10**, 4327–4335.
15 X. Peng, W. Wang, W. Yang, J. Chen, Q. Peng, T. Wang, D. Yang, J. Wang, H. Zhang and H. Zeng, *J. Colloid Interface Sci.*, 2022, **618**, 111–120.
16 Q. Wang, Q. Zhang, G. Wang, Y. Wang, X. Ren and G. Gao, *ACS Appl. Mater. Interfaces*, 2022, **14**, 1921–1928.
17 Y. Zhang, E. Ren, A. Li, C. Cui, R. Guo, H. Tang, H. Xiao, M. Zhou, W. Qin, X. Wang and L. Liu, *J. Mater. Chem. B*, 2021, **9**, 719–730.
18 X. Fan, Y. Fang, W. Zhou, L. Yan, Y. Xu, H. Zhu and H. Liu, *Mater. Horiz.*, 2021, **8**, 997–1007.
19 Z. Gao, L. Kong, R. Jin, X. Liu, W. Hu and G. Gao, *J. Mater. Chem. C*, 2020, **8**, 11119–11127.
20 M. Liao, P. Wan, J. Wen, M. Gong, X. Wu, Y. Wang, R. Shi and L. Zhang, *Adv. Funct. Mater.*, 2017, **27**, 1703852.
21 C. Kim, H. Lee, K. Oh and J. Sun, *Science*, 2016, **353**, 682–687.
22 K. H. Kim, Y. Oh and M. F. Islam, *Nat. Nanotechnol.*, 2012, **7**, 562–566.
23 C. Larson, B. Peele, S. Li, S. Robinson, M. Totaro, L. Beccai, B. Mazzolai and R. Shepherd, *Science*, 2016, **351**, 1071–1074.
24 Z. Lei, Q. Wang, S. Sun, W. Zhu and P. Wu, *Adv. Mater.*, 2017, **29**, 1700321.
25 J. Zhang, L. Wan, Y. Gao, X. Fang, T. Lu, L. Pan and F. Xuan, *Adv. Electron. Mater.*, 2019, **5**, 1900285.
26 L. Han, K. Liu, M. Wang, K. Wang, L. Fang, H. Chen, J. Zhou and X. Lu, *Adv. Funct. Mater.*, 2018, **28**, 1704195.
27 H. Liao, X. Guo, P. Wan and G. Yu, *Adv. Funct. Mater.*, 2019, **29**, 1904507.
28 X. Liu, Q. Zhang and G. Gao, *Chem. Eng. J.*, 2020, **394**, 124898.
29 Y. Gao, Z. Zhang, X. Ren, F. Jia and G. Gao, *J. Mater. Chem. B*, 2022, **10**, 5743–5752.
30 H. Qiao, P. Qi, X. Zhang, L. Wang, Y. Tan, Z. Luan, Y. Xia, Y. Li and K. Sui, *ACS Appl. Mater. Interfaces*, 2019, **11**, 7755–7763.
31 B. Wu, Z. Mai, Z. Ji, B. Du and S. Y. Huang, *Mater. Today Phys.*, 2022, **29**, 100905.
32 P. Kalendova, L. Svoboda, J. Hroch, P. Honcova, H. Drobna and S. Slang, *Starch/Staerke*, 2021, **73**, 2100051.
33 R. Thakur, P. Pristijono, J. B. Golding, C. E. Stathopoulos, C. Scarlett, M. Bowyer, S. P. Singh and Q. V. Vuong, *Starch/Staerke*, 2017, **70**, 1700099.
34 L. A. Heinrich, *Green Chem.*, 2019, **21**, 1866–1888.
35 P. S. Shuttleworth, V. Budarin and J. H. Clark, *J. Mater. Chem.*, 2009, **19**, 8589–8593.

36 T. T. Koev, J. C. Munoz-Garcia, D. Iuga, Y. Z. Khimyak and F. J. Warren, *Carbohydr. Polym.*, 2020, **249**, 116834.
37 C. Ma, F. Xie, L. Wei, C. Zheng, X. Liu, L. Wang and P. Liu, *ACS Sustainable Chem. Eng.*, 2022, **10**, 6724–6735.
38 X. Shang, Q. Wang, J. Li, G. Zhang, J. Zhang, P. Liu and L. Wang, *Carbohydr. Polym.*, 2021, **257**, 117626.
39 S. Tavakoli, M. Kharaziha, S. Nemati and A. Kalateh, *Carbohydr. Polym.*, 2021, **251**, 117013.
40 Z. Yang, X. Chen, Z. Xu, N. Ji, L. Xiong and Q. Sun, *Int. J. Biol. Macromol.*, 2021, **190**, 382–389.
41 S. Zeng, J. Zhang, G. Zu and J. Huang, *Carbohydr. Polym.*, 2021, **267**, 118198.
42 J. Lu, O. Hu, L. Hou, D. Ye, S. Weng and X. Jiang, *Int. J. Biol. Macromol.*, 2022, **221**, 1002–1011.
43 K. Gonzalez, C. Garcia-Astrain, A. Santamaria-Echart, L. Ugarte, L. Averous, A. Eceiza and N. Gabilondo, *Carbohydr. Polym.*, 2018, **202**, 372–381.
44 I. Gholamali and M. Yadollahi, *Int. J. Biol. Macromol.*, 2020, **160**, 724–735.
45 Q. Lin, H. Li, N. Ji, L. Dai, L. Xiong and Q. Sun, *Carbohydr. Polym.*, 2021, **251**, 116982.
46 K. Depa, A. Strachota, M. Šlouf and J. Brus, *Eur. Polym. J.*, 2017, **88**, 349–372.
47 C. Yang, P. Zhang, A. Nautiyal, S. Li, N. Liu, J. Yin, K. Deng and X. Zhang, *ACS Appl. Mater. Interfaces*, 2019, **11**, 4258–4267.
48 D. Liu, H. Zhou, Y. Zhao, C. Huyan, Z. Wang, H. Torun, Z. Guo, S. Dai, B. B. Xu and F. Chen, *Small*, 2022, **18**, e2203258.
49 G. Ge, Y. Z. Zhang, W. Zhang, W. Yuan, J. K. El-Demellawi, P. Zhang, E. Di Fabrizio, X. Dong and H. N. Alshareef, *ACS Nano*, 2021, **15**, 2698–2706.
50 Y. Z. Zhang, J. K. El-Demellawi, Q. Jiang, G. Ge, H. Liang, K. Lee, X. Dong and H. N. Alshareef, *Chem. Soc. Rev.*, 2020, **49**, 7229–7251.
51 Y. Zhang, K. Lee, D. H. Anjum, R. Sougrat, Q. Jiang, H. Kim and H. N. Alshareef, *Sci. Adv.*, 2018, **4**, eaat0098.
52 H. Luan, D. Zhang, Z. Xu, W. Zhao, C. Yang and X. Chen, *J. Mater. Chem. C*, 2022, **10**, 7604–7613.
53 M. L. Hammock, A. Chortos, B. C. Tee, J. B. Tok and Z. Bao, *Adv. Mater.*, 2013, **25**, 5997–6038.
54 Y. Ma, Y. Cheng, J. Wang, S. Fu, M. Zhou, Y. Yang, B. Li, X. Zhang and C. W. Nan, *InfoMat*, 2022, **4**, e12328.
55 A. Olad, F. Doustdar and H. Gharekhani, *Colloids Surf., A*, 2020, **601**, 124962.
56 B. Bulkin, Y. Kwak and I. Dea, *Carbohydr. Res.*, 1987, **160**, 95–112.
57 S. Anjum, P. Gurave, M. V. Badiger, A. Torris, N. Tiwari and B. Gupta, *Polymer*, 2017, **126**, 196–205.